Numerical and experimental performance study of two-degrees-of-freedom electromagnetic energy harvesters

Energy Conversion and Management: X 18 (2023) 100348

Contents lists available at ScienceDirect

Energy Conversion and Management: X

journal homepage: www.sciencedirect.com/journal/energy-conversion-and-management-x

Numerical and experimental performance study of two-degrees-of-freedom electromagnetic energy harvesters

M. Lo Monaco *, C. Russo, A. Somà

Department of Mechanical and Aerospace Engineering, Politecnico di Torino, Corso duca degli Abruzzi 24, Torino 10129, Italy

ARTICLE INFO

Keywords:
Electromagnetic energy harvesting
Magnetic spring
Transducers
Numerical modeling
Experimental tests
Autonomous internet of things

ABSTRACT

Energy harvesting is a rising technology able to replace conventional batteries in supplying low-power devices. Researchers are studying the use of energy harvesters in Autonomous Internet of Things (AIoT) systems to create a wireless network of nodes for real-time monitoring of assets. Electromagnetic energy harvesters exploiting ambient vibrations for electric power generation are used in monitoring applications for sensorized industrial vehicles or mechanical systems. This paper shows a design methodology for two-degrees-of-freedom gravitational electromagnetic energy harvesters (2DOF GEMEHs) along with prototype testings. The main purpose of this non-linear two-degrees-of-freedom system is to improve conversion efficiency and bandwidth broadening through the introduction of a second resonance frequency. The proposed harvester devices could be suited for vehicle monitoring and in particular railway monitoring applications. The novelty of the configuration is the use of two magnetic springs and the series connection of two induction coils. The system design achieves long-lasting performances since there are no mechanical parts involved in the dynamics, thus being compatible with low maintenance requirements. 2DOF GEMEHs can have the two resonance frequencies tuned to two fundamental frequencies of the vehicle harvested vibrations for power enhancement. Infreight trains applications the system resonance frequencies may be tuned to the two natural frequencies of the bogie when the railcar is in tare and loaded conditions. The working principle, configuration and analytical model of these devices are described in a detailed way. The numerical modeling approach consists of a combination of FEM analyses in Ansys Maxwell and dynamic simulations in Simulink for evaluation of stiffness and damping characteristics of the system. Experimental laboratory tests on harvester prototypes are compared to numerical results of dynamic simulations for the validation of the proposed model through error estimation. Performance improvements of the 2DOF GEMEH are evaluated through the definition of a merit factor based on output power and bandwidth. The use of a 2DOF system is justified by comparing its efficiency respect to the 1DOF configuration, leading to an overall harvesting performance improvement of 10%.

1. Introduction

The Internet of Things (IoT) technology is an increasingly growing trend in a wide range of applications and fields [1]. The major challenge is finding a reliable and adequate power supply, raising the researchers' interest in sustainable options. Energy harvesting is a promising technique that converts the unused ambient energy into electric energy. The use of energy harvesters and wireless sensors creates a network of Autonomous Internet of Things (AIoT) devices that can realize Condition-Based Maintenance and Digital Twins [2–4]. Moreover, the use of energy harvesters can be a solution in systems that do not guarantee the supply of electricity. For this reason, the researchers are interested in applying AIoT systems in freight vehicles for structural monitoring to overcome the absence of onboard electric power [5]. In literature, there are many research works regarding the design and study of energy harvesting devices in the railway field. The authors' research group has been studying energy harvesting solutions for IoT applications for the last decade. The works are focused on one-degree-of-freedom

Abbreviations: IoT, Internet of Things; AIoT, Autonomous Internet of Things; DOF, Degree of Freedom; GEMEH, Gravitational ElectroMagnetic Energy Harvester; AUC, Area Under the Curve; FEM, Finite Elements Method; DAQ, Data Acquisition System; FRF, Frequency Response Function; RMS, Root Mean Square; NPD, Normalized Power Density.

* Corresponding author.
E-mail address: mirco.lomonaco@polito.it (M. Lo Monaco).

https://doi.org/10.1016/j.ecmx.2023.100348

Available online 6 January 2023

electromagnetic energy harvesters for wearable applications and for industrial vehicles monitoring [5–7]. The ongoing research of the authors has led to recent publications [8,9]. This paper reports the design methodology of two-degrees-of-freedom gravitational electromagnetic energy harvesters (2DOF GEMEHs). Electromagnetic energy harvesters exploit mechanical energy coming from ambient vibrations for generation of electric power. The main transducing techniques use magneto-induction or piezoelectric materials. The maximum power conversion happens at the resonance frequency of the electromagnetic energy harvester. For this reason, the main design issue is the tuning of the resonance frequency with the main excitation frequencies coming from ambient vibrations, depending on the monitored system on which the harvester is installed. Vehicle monitoring and in particular railway monitoring could be one of possible applications of the harvesting devices. Gravitational electromagnetic energy harvesters use magnetic springs based on the magnetic levitation principle instead of traditional mechanical springs. The characteristic of magnetic springs is a low stiffness and consequently low frequency resonance conditions [10]. This is compatible with the railway applications, as the primary and secondary suspensions of the train bogies filter the vertical vibrations coming from wheel-railroad contact. The wagon major vertical excitation frequencies are in the range from 1 to 20 Hz, depending on the type of boogie, train speed, railroad conditions and carried weight [5,11,12]. The following design challenges are the reduction of the system size and, consequently, the increase of the power density, as well as the broadening of the bandwidth around resonance. Researchers are studying different strategies for increasing the operating frequency range of vibration energy harvesters, [13,14]. The most common solution is the use of non-linear springs to change the shape of the Frequency Response Function of the system and increase power generation. Magnetic springs present a strong non-linear behavior even though introduce design difficulties and limits. The study of a two-degrees-of-freedom system has the purpose of broadening frequency bandwidth at high power with respect to a 1DOF system, by the introduction of another resonance frequency. Researchers have come to the conclusion that higher DOFs configurations are capable of harvesting energy over a wider frequency range, accepting lower maximum output [15]. In particular, 2DOF systems can be useful in applications that have two main excitation frequencies on which the harvesters can be tuned through proper design of the two DOFs mass ratios and stiffnesses. The mass ratio of the two moving masses is a relevant design variable as it influences the tuning activity by modifying the resonance frequencies and power generation. Ung et al. [12] realize a two-degrees-of-freedom electromagnetic harvester using coupled oscillating systems for structural health monitoring of a heavy haul railcar. The harvester is tuned with the fundamental vibration frequencies of the wagon when loaded and unloaded, 6.4 Hz and 14.5 Hz respectively. The device generates peak output powers of 212 mW and 218 mW from sinusoidal vibration with 0.4 g peak acceleration at the two resonance frequencies. The work of Rodriguez et al. [16] shows a two-degrees-of-freedom velocity-amplified electromagnetic vibrational energy harvester (EMEH). The device uses magnetic springs and has the peculiar feature of adjustable tube length, thus changing and adapting the harvester resonance frequencies to the destined application. Fan K. et al., [17] study a 2DOF EMEH to scavenge energy coming from ultra-low frequency excitations of human motion. The device is composed of a magnetically levitated 1DOF EMEH that can oscillate relatively inside an external moving cylindrical enclosure. The work of Feng et al. [18] regards a 2DOF energy harvester that uses a serpentine planar spring. The system has an enhanced "band-pass" harvesting characteristic compared to a conventional dual-resonance system. The device generates an output power of 11 mW at the first resonance frequency of 58 Hz, 14.9 mW at the second resonance frequency of 74.5 Hz. Ahmad et al. [19] propose a two-degrees-of-freedom system with dual electromagnetic transduction mechanisms incorporated in a cantilever beam. The device exploits the beam two main resonance frequencies of its vibration mode shapes for maximum velocities of the magnets and output power generations. The sum of the two magnetic transducers generates, for an external acceleration input of 0.09 g amplitude, 2.51 mW at first resonance frequency of 4.4 Hz and 10.7 mW at second resonance of 5.5 Hz. Zhang et al. [20] work studies a two degree of freedom electromagnetic vibration energy harvesting system having an Halback array type of magnet arrangement. The device generates a peak power of 25 mW at first resonance frequency of 6.2 Hz but a significantly lower peak of about 5 mW at the second resonance frequency of 14 Hz. The work of Foisal et al. [21] regards a multi-frequency electromagnetic energy harvester composed of an array of four transducers having magnetic springs. The system achieves a power density of 52.02 W/cm^3 at an acceleration of 0.5 g.

This paper is a research study on cylindrical two-degrees-of-freedom gravitational electromagnetic energy harvesters (2DOF GEMEHs), having two magnetic springs in series. This configuration consists of a tube with coils wrapped on the external surface and three co-axials cylindrical magnets having repulsive forces. The main purpose of this work is to study the performance improvements in terms of output power and frequency bandwidth of a novel 2DOF electromagnetic energy harvester. Many researchers introduce other degrees of freedom by adding more proof masses without magnetic properties ([16,22,23]) or using complex designs having mechanical parts such as planar springs [18], helicoidal springs ([12,20]) or cantilever beams [19]. Most of the analyzed devices can be destined only to laboratory testing since they are in a prototyping stage, whereas the device in this work is designed for real applications in the railway field. The novelty of the proposed configuration lies in the use of two magnetic suspensions in series and, consequently, two magneto-inductive sources. The use of two oscillating permanent magnets enhances the resulting magnetic flux linkage through two coils, one per magnet, that are connected in series. Moreover, the novel device has low-cost and long-lasting design due to the absence of any mechanical part involved in the dynamics, [24]. The application of these devices is to harvest ambient vibrations for supplying wireless sensor nodes for condition-based monitoring of unelectrified freight wagons. The 2DOF GEMEH complies with trains installation requirements [6,10], especially of low maintenance, highlighting its in-field applicability. The device is installed on the bogie in the vertical direction to harvest the wheel-railroad vibrations on the z-axis. GEMEHs are well-suited power generators for this application since the use of magnetic suspension results in a non-linear spring having low resonance frequency (1–50 Hz, [25]). GEMEHs are novel even among energy harvesters that use magnetic suspensions since most researchers have magnetic springs with symmetric layouts, [17,21]. GEMEHs present asymmetric magnetic suspensions, due to the absence of the top magnet, that enable longer strokes of the magnet and consequently reduce the system resonance frequency. The proposed design has the lowest resonance frequencies in literature (3.4 Hz, 6.7 Hz), confirming its suitability for freight wagons.

The paper describes the design phases of the device and the validation through experimental tests. Firstly, the structure of the energy harvester is described justifying the choice of the two masses. Secondly, the analytical and numerical models in Matlab/Simulink environment are proposed with the support of Ansys Maxwell FEM software. Then, the results of experimental laboratory tests on harvester prototypes are compared with the simulation results with brilliant matching. The last section discusses 2DOF GEMEH performance enhancements respect to 1DOF system and similar devices in literature, concluding with its advantages and future optimization works.

2. Materials and methods

2.1. Harvester configuration

The main components of a 2DOF GEMEH are three coaxial ring permanent magnets, two suspended and one fixed at the bottom, creating a series of two magnetic springs and coils wrapped around a

tube having circular cross-section area. The moving magnets during their vertical oscillation generate variable magnetic fluxes, inducing an electromotive force in the coils, and return to their equilibrium positions under gravitational force. Peak power is generated when the external excitation frequency is equal to the resonance frequency of one of the moving magnets. Consequently, the dimensioning of these generators is strictly dependent of their applications for frequency tuning. Using a non-linear stiffness broadens the frequency range around the resonance frequency, thus increasing the system efficiency. The peculiarity of the devices studied in this paper lies in the asymmetry of the magnetic suspension, given that only one fixed magnet is present at the bottom of the tube. The absence of the top fixed magnet enables a longer stroke for the moving magnets, resulting in a stiffness that is lower than the symmetrical suspension. The purpose of introducing a second degree of freedom with an additional non-linear stiffness and magneto-inductive properties is to further increase the high-power frequency range and overall power generation.

The 2DOF GEMEH configuration is similar to a dynamic vibration absorber. Fig. 1 shows the system schematic representation, highlighting the interaction between the magnets and the external forces. One of the main design variables is the mass ratio of the two moving magnets, since it has a direct influence on the harvester performances. Experimental tests are performed on different prototypes to evaluate the relation between the mass ratio and the frequency bandwidth and output power. Starting from a 1DOF configuration having optimum design variables (magnet dimensions m_1, tube length, coil positions and number of turns, resistive load), different top masses (referred to as m_2) are tested and the corresponding output power Frequency Response Functions (FRFs) are computed for comparison.

The 1DOF design and dimensions are the result of the continuation of preliminar studies of our research group, [8]. Fixed magnet and m_1 dimensions are chosen for resonance frequency tuning to the fundamental excitation frequencies of freight train Multibody simulations [5]. The tested mass ratios in the 2DOF configuration $\chi = m_2/m_1$ are 0.25, 0.5, 0.75, 1 and the harvesters prototypes are referred to as EH1, EH2, EH3, EH4 respectively. The magnets are composed of modular units having the same diameter and height, being stackable thanks to the attraction forces. m_1 is composed of four units and configurations going from EH1 to EH4 have m_2 made from one to four units respectively. The fixed magnet is the same for all the four configurations and is made of only one unit. Fig. 2 shows the schematic representation of the four tested configurations. The system does not behave as a simple dynamic absorber since the springs are magnetic and not mechanical. This means that changing the magnet masses and size also effects the stiffness, damping and electromagnetic coupling coefficient values of both DOFs because are directly related to the magnetic moment of the moving magnets. The experimental results of this analysis are thoroughly discussed in Section 4.2. Amongst all the configurations, EH3 having the mass ratio $\chi = 0.75$ shows the best merit factor depending on peak power amplitude, area under the curve magnitude and frequency bandwidth broadening. This configuration is used for the complete non-linear numerical modeling described in the following sections and compared to the experimental results for validation. Fig. 3 represents EH3 schematics giving further details on the main dimensions and characteristics of the components.

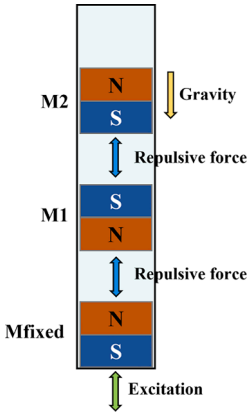

Fig. 1. Schematic representation of the 2DOF GEMEH and acting forces.

The tube design presents a radial clearance (about 0.2 mm) between the moving magnets and internal tube surface to consent the correct vertical motion of the magnets along their axis of symmetry. On the other hand, this design yields undesired transversal motions and impacts. Using ring magnets and an internal guide reduces the drawbacks and correctly directs the vertical motion of the masses, preventing the performances decrease. Ten coils are wrapped around the tube, all made of enameled copper wires and having same dimensions, number of turns, wire diameter and resistance. The coils are placed along the tube at different positions in the vertical direction, in order to find the optimum coil axial location for maximum power generation. The optimum coil location is where there is maximum flux linkage during the motion of the moving magnets. The coils radial and longitudinal dimensions, along with the number of turns and resistance, is optimized by simulation tests of the moving magnets flux. The two moving magnets oscillate around each equilibrium position which are far enough to decouple the electromagnetic interaction between each mass. m_1 oscillates around the lower part of the tube, inducing a voltage in the lower coils 1 to 4, whereas m_2 oscillates around the upper part of the tube and induces a voltage in the upper coils 7 to 10 (see Fig. 3). Consequently, the optimum coil for each moving magnet can be evaluated considering the decoupled induction effects. These two optimum coils can then be connected in series to couple the induced voltages and maximize the harvester performances. The table in Fig. 3 reports the optimized electrical variables of the system. All the magnets in the device are made of NdFeB-N42.

2.2. Analytical model

From an analytical point of view, the harvester can be considered as a 2DOF non-linear mass-spring-damper system. The seismic masses m_1 and m_2 along with the fixed magnet at the bottom end of the tube generate two magnetic suspensions in series. The moving magnets m_1 and m_2 are suspended because of the repulsive force acting between them, as Fig. 1 shows. The first magnetic suspension, connecting the fixed magnet and m_1, has a non-linear stiffness k_1, while the second suspension, connecting m_1 and m_2, has a non-linear stiffness k_2. The magnetic force between m_2 and the fixed magnet is neglected because their relative distance is significantly large, [17]. The damping characteristics of the two magnetic suspensions have two components: mechanical due Coulomb friction and viscous action of the air (c_{vis}), electromagnetic due to the induction of parasitic currents in the coils (c_{em}). The mechanical damping of the second suspension in the model (c_{vis2}) acts between the two masses as its effect depends on their relative oscillations. Electromagnetic dampings (c_{em}) effects, instead, depend on the oscillation of the masses relatively to the fixed coils, hence they act between each mass and the base. An external sinusoidal excitation is applied to the system base, driving the oscillation motions of the two moving magnets. The relative motion of the two magnets inside the tube respect to the fixed coils creates a time-variating magnetic flux and, therefore, an induced electromotive force, executing the transducing mechanism of the device. The analytical model of the mechanical subsytem is shown in Fig. 4a. The electromagnetic subsystem needs to be studied and to be coupled with the mechanical one to evaluate the transducing mechanism and quantify the power generation. The main electromagnetic characteristics of the harvester are the electromagnetic damping and coupling coefficient. These physical quantities present a non-linear behavior as they depend on the time variation of the magnetic flux linkage across the coils. The electro-mechanical coupling

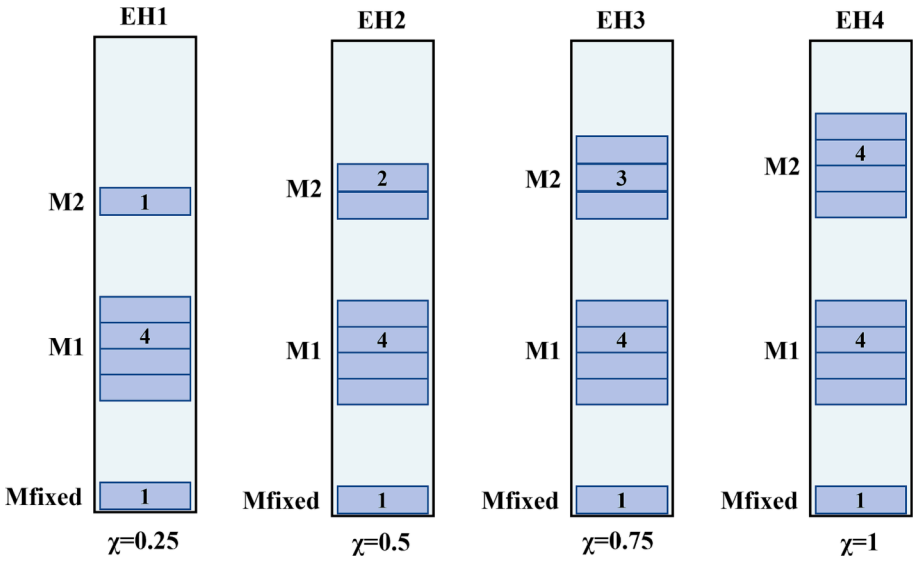

Fig. 2. Mass ratios of tested configurations EH1, EH2, EH3, EH4.

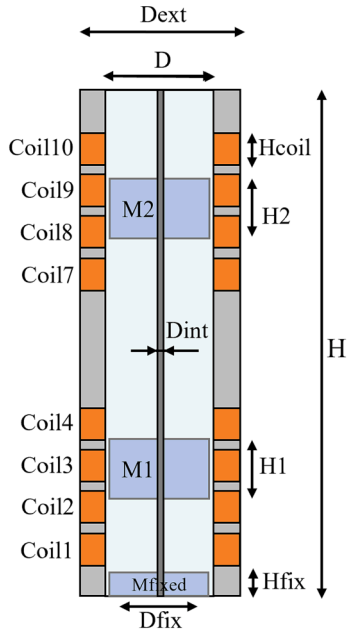

D (mm)	20
Dfix (mm)	10
H1 (mm)	20
H2 (mm)	15
Hfix (mm)	5
Dext (mm)	22
Dint (mm)	4
H (mm)	180
Hcoil (mm)	10
m1 (g)	45
m2 (g)	22.5
Dwire (mm)	0.1
Nturns	500
Rcoil (Ω)	90

Fig. 3. EH3 main components and dimensions.

derives from the direct dependence of the induced electromotive force and the generated power on the moving magnets speed and displacement. The electromagnetic circuit of the system can be modeled as one mesh where the harvester is an AC source, having internal resistance R_{coil}, connected to the external resistive load R_{load} that needs to be properly designed for maximum power generation. A schematic representation of the electromagnetic circuit of the harvester is reported in Fig. 4b. The equation of motion of each degree of freedom (1)-(2) is a time-dependent second order differential equation.

$$m_1\ddot{x}_1 + c_{em1}(\dot{x}_1 - \dot{y}) + c_{vis1}(\dot{x}_1 - \dot{y}) - c_{vis2}(\dot{x}_2 - \dot{x}_1) + k_1(x_1 - y) - k_2(x_2 - x_1) = 0 \quad (1)$$

$$m_2\ddot{x}_2 + c_{em2}(\dot{x}_2 - \dot{y}) + c_{vis2}(\dot{x}_2 - \dot{x}_1) + k_2(x_2 - x_1) = 0 \quad (2)$$

Where:

- m_1, m_2 are the seismic masses of the moving magnets
- c_{vis1}, c_{vis2} are the viscous dampinsg of DOF 1 and 2
- c_{em1}, c_{em2} are the electromagnetic dampings of DOF 1 and 2
- k_1, k_2 are the non-linear stiffnesses of the two magnetic springs
- y is the external sinusoidal movement applied to the base, having acceleration amplitude Y_0 and frequency ω

The implementation of Kirchoff's laws to the electromagnetic circuit leads to the definition of Eqs. (3)-(4).

$$i = \frac{V_{eh}}{R_{coil} + R_{load}} \quad (3)$$

$$P_{load} = V_{load} i \quad (4)$$

The electromagnetic coupling coefficient $k_{em}(z)$ derives from the variation of the magnetic flux during the moving magnet oscillation (6). The coefficient directly links the voltage to the moving magnet speed (7) and defines the electromagnetic damping force acting on the moving mass (8)-(9). Eqs. (6)–(9) are solved for each of the two moving magnets separately, deriving the two decoupled damping and coupling coefficient characteristics and, consequently, output voltage and power.

$$k_{em}(z) = -\frac{d\Phi}{dz} \quad (5)$$

$$V_{eh} = -\frac{d\Phi}{dt} = -\frac{d\Phi}{dz}\frac{dz}{dt} = k_{em}\dot{z}(t) \quad (6)$$

$$F_{em} = k_{em}(z) * i(t) = k_{em}^2(z) * \frac{\dot{z}(t)}{R_{coil} + R_{load}} = c_{em}(z) * \dot{z}(t) \quad (7)$$

$$c_{em}(z) = \frac{k_{em}^2(z)}{R_{coil} + R_{load}} \quad (8)$$

Eqs. (1)-(8) are implemented in a MATLAB/Simulink model used for system dynamics simulations. The solution return as output variables the moving magnets position, speed, acceleration and the total induced voltage, current and generated power on the electrical load for each time step. The Simulink block scheme is shown in Fig. 5. The model is split into three subsystems, two of which are the mechanical subsystems solving the equations of motion of each degree of freedom, while the third solves the electromagnetic subsystem. The electro-mechanical coupling of the three subsystems allows to obtain the output electrical variables as solutions by applying an external mechanical sinusoidal

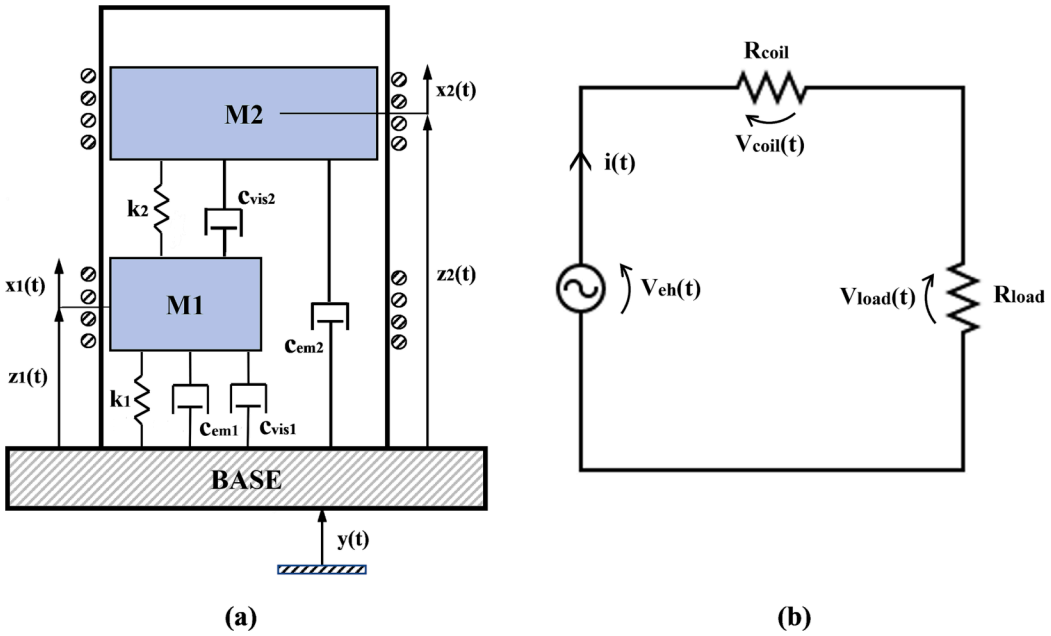

Fig. 4. Analytical model of the mechanical (a) and electromagnetic (b) subsystem.

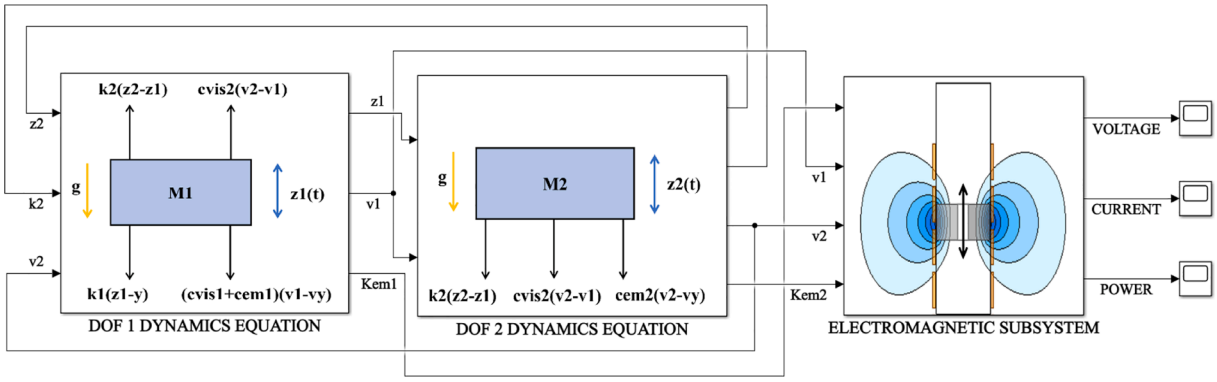

Fig. 5. Simulink model.

input. Eq. (7) describes the computation of the induced electromotive force of each magnet, following the above-mentioned decoupling considerations in Section 2.1. The dynamic equations of the two magnets are expressed in the variable z_1 and z_2, which are the motion coordinates of m_1 and of m_2 relative to the base motion y having origin in each equilibrium position, respectively.

The stiffness and damping non-linear characteristics need to be defined and inserted in the Simulink model as 1D Look-up Table blocks. These characteristics can be obtained through numerical simulations in Ansys Maxwell software and subsequently interpolated by the best fitting functions. Ansys Maxwell is a FEM-based software used for electromagnetic field simulations in static and dynamic systems, both in time and frequencies domain for bi-dimensional and tri-dimensional geometries. The numerical model of the harvester is built in Ansys Maxwell environment for magnetostatic and transient electromagnetic simulations of the magnetic suspensions field. Given the axisimmetry of the system a 2D model in cylindrical coordinates is sufficient. A mesh convergence study is carried out to evaluate the best trade-off between precision and computational time. For this research activity the 2020 R2 Ansys version is used.

2.2.1. Mechanical model

The main mechanical characteristics of the harvester are the stiffnesses $k1, k2$ and the viscous dampings c_{vis1}, c_{vis2} of the two magnetic suspensions. The stiffness of a magnetic spring derives from the magnetic force exchange between two permanent magnets. The evaluation of the magnetic field and force inside the tube can be performed through magnetostatic analyses in Ansys Maxwell environment. Considering a 1DOF system where only one magnetic spring is present, the moving magnet is sweeped with a fine step along the height of the tube, starting from the fixed magnet upper face until the upper end of the tube. For each position of the moving magnet, Ansys Maxwell plots the distribution of magnetic field vectors, as can be seen in Fig. 6, and computes the corresponding coenergy $W(x)$ of the system. The step size of this analysis is set as 0.5 mm after a trade-off analysis between computational time and the quality of the data. Coenergy is a non-physical quantity having energy units that can be exploited for the definition of the magnetic force in the system. The derivation of the coenergy data respect to the suspendend mass position results in the magnetic repulsive force acting between the two magnets [26]. The force data coming from the numerical Maxwell model is then interpolated by the best fitting function.

$$F_{mag}(x) = \frac{dW(x)}{dx} \tag{9}$$

The magnetic force acting between two coaxial magnetic dipoles having same magnetic moment is proportional to $1/x^4$, [27]. Although the three

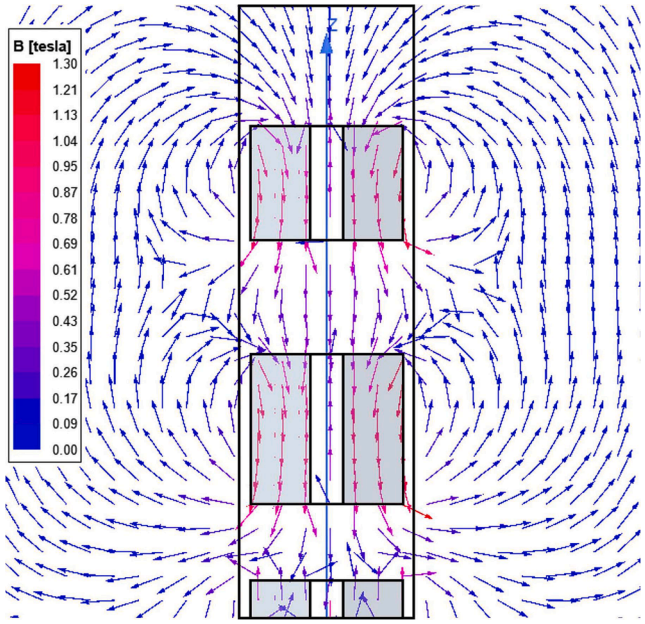

Fig. 6. Magnetic field vector of EH3.

magnets have different magnetic moments due to their different axial dimensions, the proposed function fits the simulation data quite precisely. The expression of the function is the following:

$$F_{mag,fit}(x) = \frac{p_1}{x^4 + q_1x^3 + q_2x^2 + q_3x + q_4} \tag{10}$$

The coefficients are determined in MATLAB environment. The stiffness characteristic can be simply obtained by deriving again the magnetic force fitting function respect to the absolute coordinate of the moving magnet x.

$$k(x) = \frac{dF_{mag,fit}(x)}{dx} \tag{11}$$

The transition from a 1DOF system to a 2DOF system complicates the numerical model, as two magnetic suspensions in series connection are present. The two stiffnesses of the magnetic springs are computed one at a time using different approaches. The stiffness of the second suspension, acting between the two moving magnets, is studied first. The numerical simulation is performed by sweeping m_2 position relatively to m_1, starting from its upper face, when the two magnets ideally touch, and ending to the upper face of the tube. Magnet m_1 is kept in a fixed position at a sufficient distance from the fixed magnet at the base, following the assumption of negligible interaction between m_2 and the fixed magnet. The result is k_2 non-linear stiffness characteristic that depends on the relative position between the two moving magnets. Secondly, the first magnetic suspension acting between m_1 and the fixed magnet is studied. The numerical simulation is performed by sweeping m_1 position from the upper face of the fixed magnet at the base, keeping m_2 fixed in its equilibrium position respect to m_1, until m_2 upper face reaches the upper end of the tube. Fig. 7 shows the plot of the magnetic forces of m_1 and m_2 fitting curves respect to the absolute coordinates x_1 and x_2 compared to the Maxwell simulation data for EH3. Fig. 8 reports the stiffness characteristics of the two magnetic springs and used in the Simulink model for dynamic simulations of EH3 configuration. The computation of the magnets equilibrium positions can be done by analizing the static equation for each degree of freedom. Equilibrium position of m_2 can be evaluated by finding the absolute coordinate x_{02} at which the magnetic force function between m_1 and m_2 equals m_2 weight.

$$F_{mag2,fit}(x_{02}) = F_{02} = m_2g \tag{12}$$

Equilibrium position of m_1 can be evaluated by finding the absolute coordinate x_{01} at which the magnetic force function between m_1 and fixed equals the sum of m_1 and m_2 weights.

$$F_{mag1,fit}(x_{01}) = F_{01} = (m_1 + m_2)g \tag{13}$$

The equilibrium positions values are referred to the upper face of the fixed magnet at the bottom end of the tube. Each degree of freedom of the system can be linearized by evaluating the stiffness in the equilibrium position k_{01}, k_{02} and the corresponding linear resonance frequency

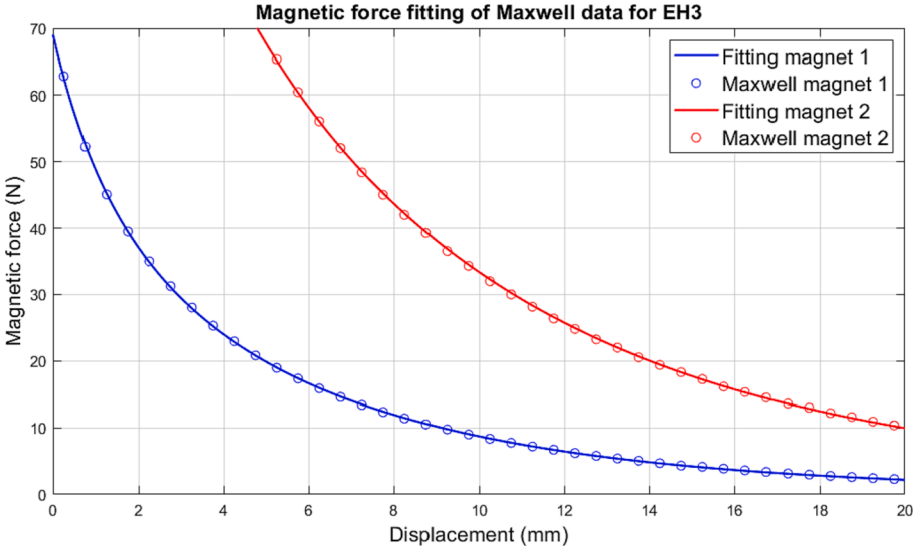

Fig. 7. Magnetic force fitting curves for EH3.

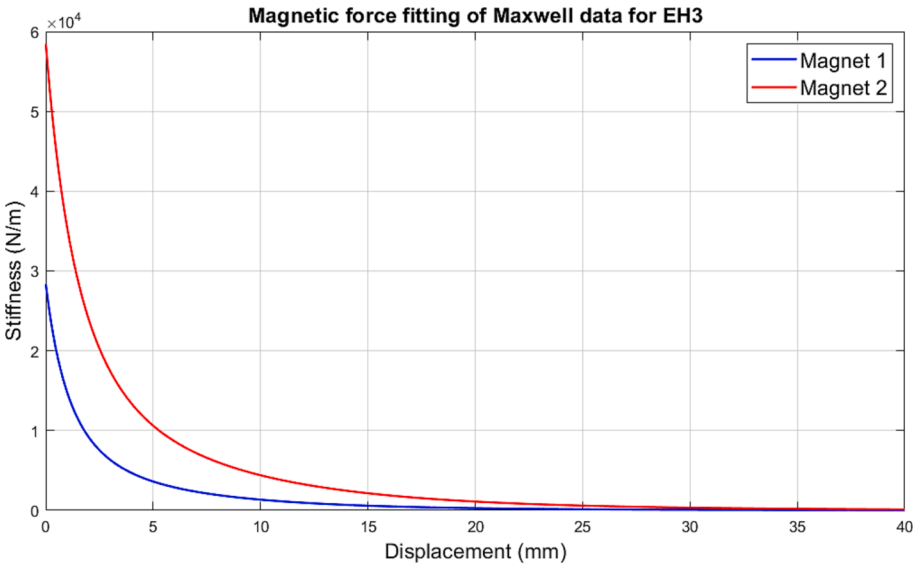

Fig. 8. Stiffness characteristics of EH3.

Table 1
Static analyses results.

x_{01} (mm)	k_{01} (N/m)	f_{res1} (Hz)	x_{02} (mm)	k_{02} (N/m)	f_{res2} (Hz)
33.4	76.4	6.6	119.4	17.2	3.6

Table 2
Viscous damping values of EH3 DOF 1 and 2.

c_{vis1} (Ns/m)	ζ_{vis1}	c_{vis2} (Ns/m)	ζ_{vis2}
0.055	0.015	0.116	0.076

f_{res1}, f_{res2}. Table 1 summarizes the main results of static analyses for EH3.

The second mechanical characteristic is viscous damping due to air action and surface friction of the moving magnets. It can be considered as a constant and evaluated through experimental tests on the devices. Free fall tests are performed on the dynamic experimental workbench (described in Section 2.3) and the harvester time response of output voltage signal is processed to extract the damping value. The peaks of the output signal are interpolated with an exponential function of time:

$$y = ae^{-b_{1,2}t} \tag{14}$$

where b is the exponential decay constant that allows to evaluate the viscous damping [15].

$$c_{vis1,2} = 2m_{1,2}b_{1,2} \tag{15}$$

The tests are performed for one magnetic spring at a time. Firstly, free fall tests of m_1 are performed without m_2 to evaluate the viscous damping value for the DOF 1. The output voltage signal is interpolated by the exponential decay function, evaluating b_1 costant for m_1 and consequently c_{vis1}. The result of this analysis are shown in Fig. 9 for DOF 1 of EH3. The same process is followed for the second magnetic suspension performing free fall tests of m_2 to compute b_2 and obtain c_{vis2} value. Table 2 shows the obtained values of viscous damping for the three configurations and the corresponding damping factor computed following this formula:

$$\zeta_{vis1,2} = \frac{c_{vis1,2}}{c_{crit1,2}} = \frac{c_{vis1,2}}{2\sqrt{k_{01,2}m_{1,2}}} \tag{16}$$

The results show that DOF 2 has a viscous damping value about two times higher than DOF 1. This may be related to the greater air friction in the tube section in between the two magnets due to their relative os-

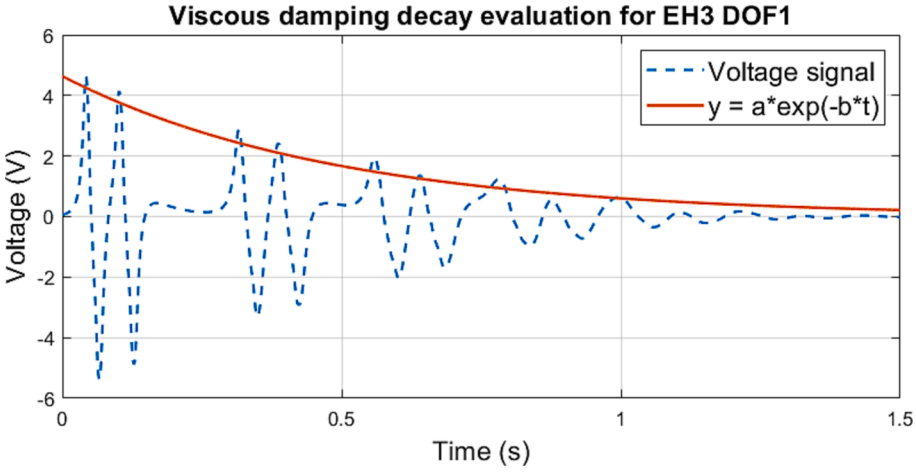

Fig. 9. EH3 exponential decay for viscous damping of DOF 1.

cillations.

2.2.2. Electromagnetic model

The main electromagnetic characteristics of the harvesters are the electromagnetic damping and coupling coefficient. These non-linear physical quantities depend on the time variation of the magnetic flux linkage across the coils. The induced electromotive force is directly dependent on the moving magnet speed, hence the mechanical and electromagnetic subsystems are strongly coupled. As described in Section 2.2, for a 1DOF system, the electromagnetic coupling coefficient $k_{em}(z)$ is derived from the variation of the magnetic flux during the moving magnet oscillation (5). The coefficient allows to link the voltage to the moving magnet speed (6) and define the electromagnetic damping force acting on the seismic mass (7)-(8). Transient simulations in Ansys Maxwell enable to evaluate the magnetic flux linkage across the harvester windings. The most efficient way to build the coils model in Maxwell is to consider them as hollow continuous cylinders. Boundary condition of "Coil" is then applied to these cylinders, allowing to insert the number of turns and the direction of current flow in the model. Transient simulations need a motion setup to be defined for the moving magnet. The displacement band in which the object moves is created with a length equal to the stroke of the moving magnet. The displacement step at which the magnetic flux is computed is set to 1 mm. The magnet speed is imposed as 1 mm/s, so that magnetic flux data can be easily changed from time-dependent to space-dependent. Therefore, it is possible to draw a curve that links the magnetic flux to the absolute displacement of the moving magnet for each coil. Considering that all the coils in each configuration are the same, the curves are identical but shifted along the x-axis due to the different axial locations of the coils. Afterwards, the electromagnetic coupling coefficient and damping can be easily determined following Eqs. (5)-(8). Coils dimensions and location along the tube need to be properly designed in order to extract the maximum amount of power from the system. Coil resistance is depending on the cross-section area and material of the wires (copper resistivity ρ_{Cu}), number of turns and mean diameter of the coil (17).

$$R_{coil} = \frac{4\rho_{Cu}}{d_{wire}^2} * d_{coil,mean} * N_{turns} \tag{17}$$

Increasing number of turns results in higher coupling coefficient but also greater damping, thus modifying the moving magnets speed and the variation of flux linkage in time. The coil location along the tube is crucial because it affects the flux linkage variation during oscillation and, consequently, the power generation. Moreover, optimum value of load resistance needs to be evaluated through load tests for maximum power generation. The experimental load tests on EH3 are reported in Section 3. In the 2DOF system, the transient simulations in Ansys Maxwell are performed for one magnet at a time to obtain the magnetic flux of each of the two masses. Subsequently, the magnetic flux curves are used to obtain the electromagnetic damping and coupling coefficient characteristics of each magnet following Eqs. (5)-(8). Figs. 10,11 show the damping and coupling coefficient curves for EH3 of m_1 and m_2 when coil 3 and coil 10 are connected one at a time. Curves for m_2 are lower in magnitude than m_1 due to its lower magnetic moment deriving from the mass ratio of 0.75. Curves for m_2 are also narrower in the induction zone of the tube around the connected coil, due to the lower height of the magnet respect to m_1.

As can be seen in Fig. 10, the coupling coefficients of the magnets are relevant only in the tube areas around each coil, whereas moving away the coefficients tens rapidly to zero. Considering the system dynamics, m_1 oscillates around the high-induction tube zone for coil 3, while m_2 oscillates around the high-induction tube zone for coil 10. The electromechanical system coupling causes the possibility to assume that if one coil from 1 to 4 is connected, then only the electromotive force of m_1 can be considered, whereas if coils 7 to 10 are connected then only the force of m_2 is significant. The next logical step is to sum the two high induction contributions of the magnets for the coils around each respective equilibrium positions. This goal can be achieved by connecting in series the two optimum coils for each of the moving magnets. Considering the induction decoupling of the two magnets, the electromotive forces produced by each magnet can be superimposed to compute the resulting electromotive force in the coil series. Consequently, Eq. (6) valid for a 1DOF circuit can be modified for a 2DOF system as follows.

$$V_{eh} = k_{em1}\dot{z}_1(t) + k_{em2}\dot{z}_2(t) \tag{18}$$

Fig. 12 shows the electromagnetic coupling coefficient curve resulting from the superimposition of m_1 coil 3 curve and m_2 coil 10 curve. These coils are experimentally confirmed to be the optimum coils for each of the two magnets respectively. The numerical model also validates this result as the equilibrium positions of each magnet coincides with the respective maximum value of the curve. Section 4.1 discusses the power enhancement of the series connection between the

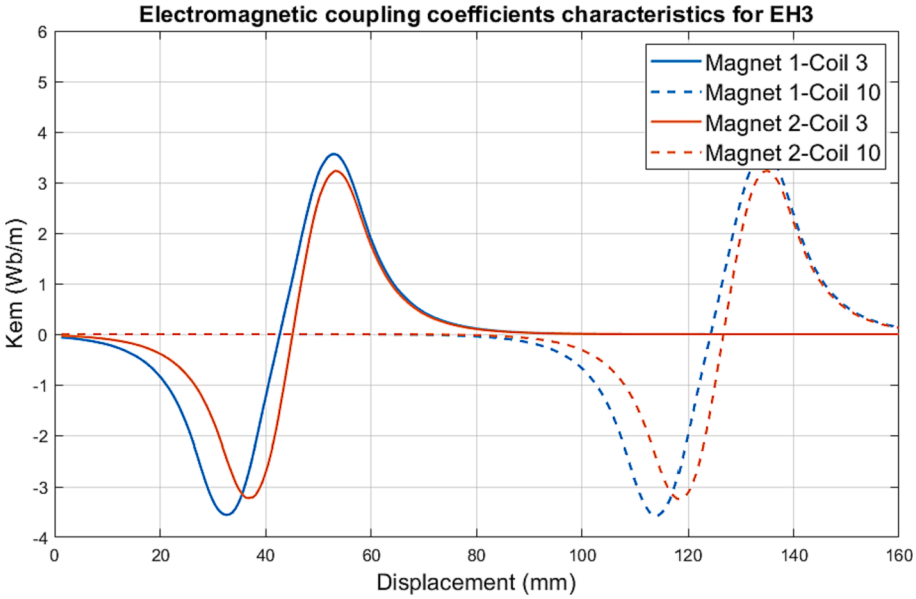

Fig. 10. EH3 electromagnetic coupling coefficient characteristics.

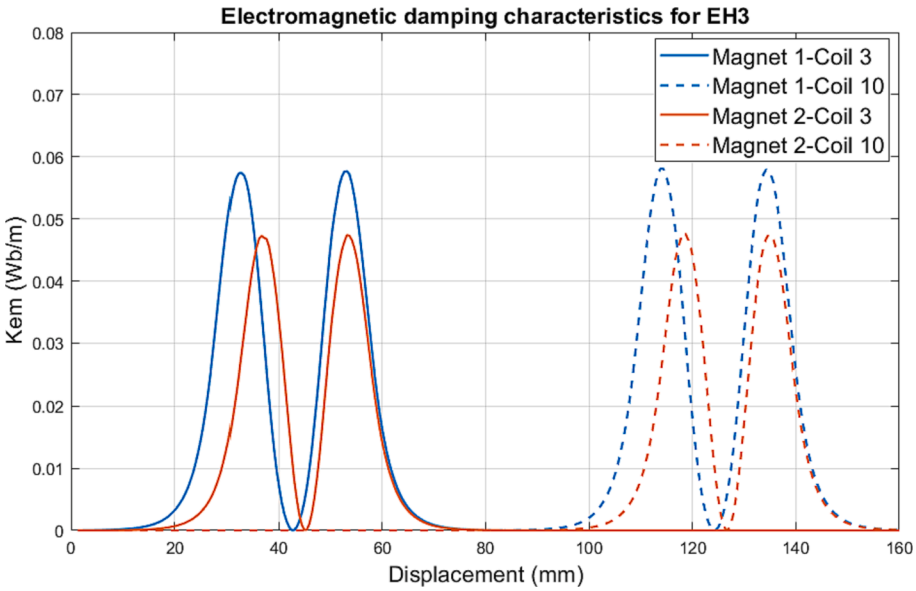

Fig. 11. EH3 electromagnetic damping characteristics.

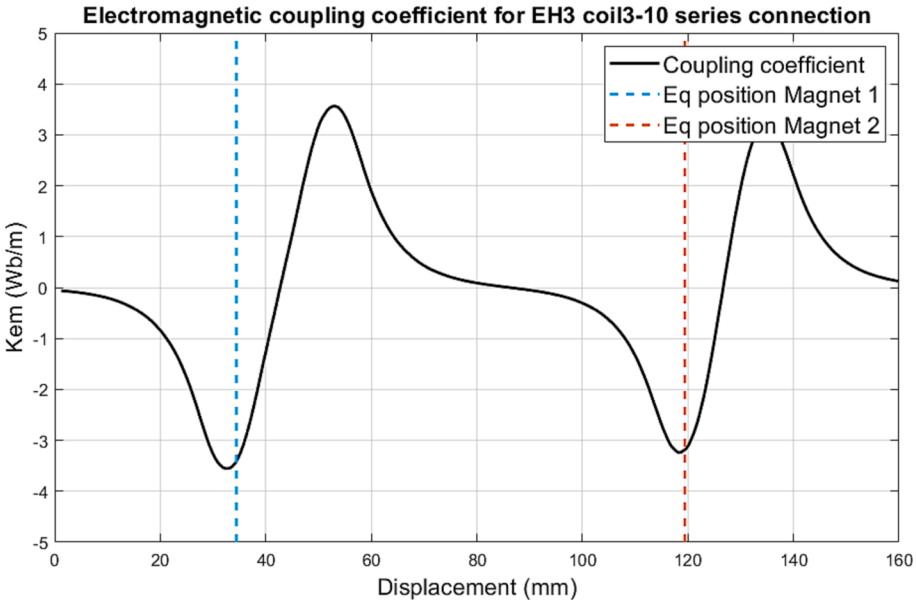

Fig. 12. Electromagnetic coupling coefficient characteristic of optimized coils series connection.

two optimum coils on the base of experimental results. Ansys software allows to plot the magnetic flux lines distributions during the motion of the suspended masses. These plots are reported in Fig. 13 placing the moving magnets in their equilibrium positions and are useful to visualize where the flux linkage is stronger and how fast it decreases moving away from the suspended magnet. Analyzing the figure it can be seen that the flux of m_1 is zero around the upper coils and viceversa for m_2, confirming again the decoupling. The flux rapidly decreases at higher radius, hence the tube width is a parameter that needs to be designed performing a trade-off between structural rigidity and amount of magnetic flux linkage.

2.3. Experimental setup

An experimental workbench is necessary to perform the dynamic tests on the devices and evaluate their performances in terms of generated power. The experimental setup logic scheme is summarized in Fig. 14 and a schematic representation is reported in Fig. 15. The energy harvester is fixed on the moving base of a shaker (TIRA TV51120) that imposes the ideal sinusoidal acceleration input. The shaker is supplied by a DAQ with LabView software (National Instruments, Austin, TX, USA) and an amplifier (BAA 500) with variable gain control (TIRA GmbH, Schalkau, Germany). A piezoelectric accelerometer (PCB Piezotronics, Depew, NY, USA) is mounted on the moving base of the shaker along with the harvester in order to provide a closed-loop feedback signal. The energy harvester output voltage signal is measured across a resistive load which can be freely changed during load tests for studying its effect on the generated power. Fig. 16 shows a rendered image of the 2DOF GEMEH which is used for prototyping and the experimental tests.

3. Simulation results and model validation

The mechanical and electromagnetic characteristics of the harvesters obtained through Ansys Maxwell numerical simulations are used in

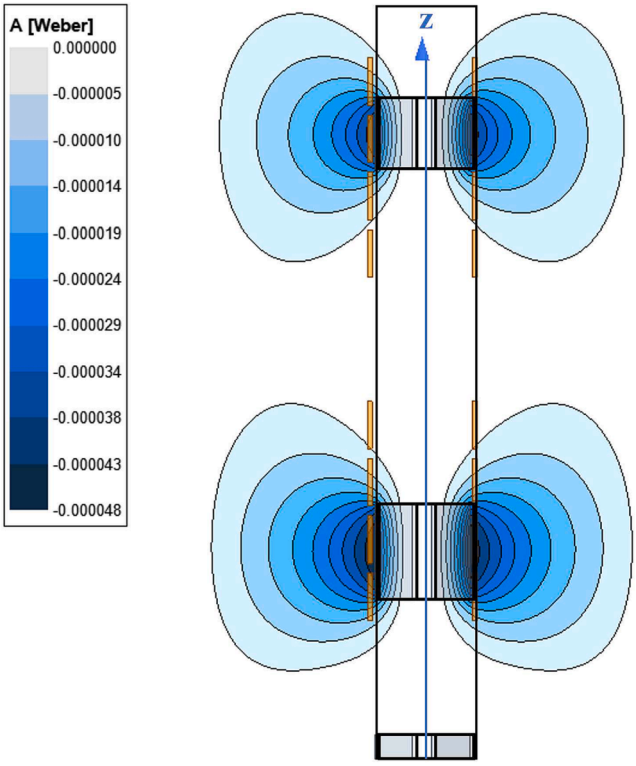

Fig. 13. Magnetic flux lines of EH3.

MATLAB/Simulink environment to perform dynamic simulations of the systems. The most relevant results of the simulations are the Frequency Response Functions (FRFs) curves that show the two resonance frequencies of the system and the relative peaks amplitude. FRFs are reported in terms of root mean square value of the generated power on the load for EH3 configuration. The FRFs are computed for the two optimum coils of EH3 (coil 3 and coil 10) and for the series connection. Table 3 summarizes the coil connections and electrical variables for computation of FRFs both for the numerical model and experimental setup. The optimum resistive loads that maximize power generation for each coil connection are obtained through experimental load tests. Fig. 17 shows the power load tests performed for EH3 coil 3, 10 and series connection 3–10, at 0.4 g excitation amplitude and resonance frequencies for maximum power generation. Experimental FRFs are obtained testing harvester prototypes on the dynamic workbench described in Section 2.3. FRFs are computed imposing a sinusoidal excitation on the shaker having an amplitude of 0.4 g and frequency sweeping from 2.5 Hz to 10 Hz with a step of 0.1 Hz. These tests are performed for all the coils of EH3 to find the optimum ones for each moving magnet.

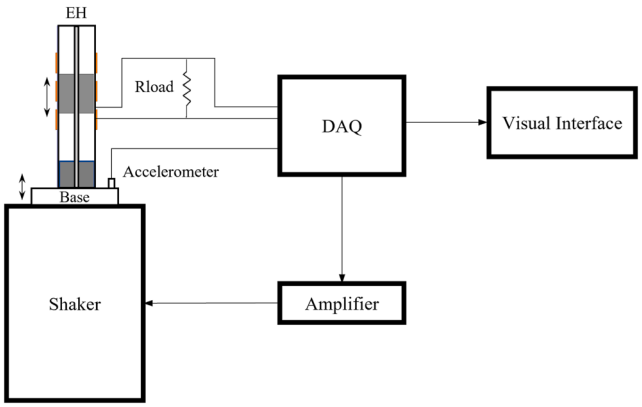

Fig. 15. Experimental setup representation.

Fig. 16. Rendered image of the 2DOF prototype.

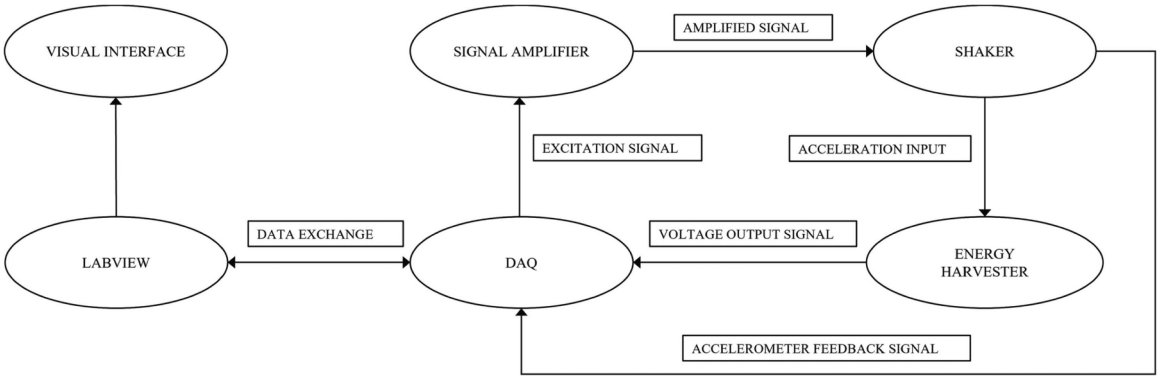

Fig. 14. Experimental setup logic scheme.

Table 3
Coils and electrical variables for tests and simulations of EH3.

Coil connection	$R_{coil}(\Omega)$	$R_{load,opt}(\Omega)$
Coil 3	90	130
Coil 10	90	130
Coil 3-10 series	180	210

The optimum coils are evaluated by comparing the peak power at the two resonance frequencies and the areas under the curves (AUC) of the RMS power FRFs. Coil 3 and coil 10 are the optimum coils respectively for m_1 and m_2, which are connected in series for maximum power generation. Section 4.1 discusses about the power enhancement of the series connection of two coils. Validation of the numerical model is a mandatory step for the design of every system. Simulation results need to be compared to experimental results of tests on harvester prototypes. A good superimposition of experimental and numerical FRFs leads to the validation of the proposed model. Figs. 18–20 report the comparison between numerical and experimental RMS power FRFs of EH3 for coil 3, 10 and 3–10 series connection respectively, applying an external excitation of 0.4 g amplitude. The superimposition of the curves visually leads to satisfactory results. As can be seen in Fig. 18, the model FRF curve follows the experimental behavior quite precisely with slight differences in the resonance peaks amplitudes. The comparison results for coil 10 in Fig. 19 show some detuning phenomenon in the resonance frequencies that may be related to the absence in the numerical model of the impact that the top magnet m_2 has with the cap in resonance conditions. The collision leads to an additional "hardening" effect to the magnetic suspension non-linear behavior that shifts the first resonance frequency, related to DOF 2, to higher values. Even though, the shifting phenomenon is still modest and does not compromise the validity of the proposed numerical model. Fig. 20 shows the comparison between experimental and numerical FRFs for the series connection of coil 3–10, pointing out a resulting brilliant superimposition.

For the purpose of quantifying the preciseness of the numerical model, a relative error between the numerical and the experimental results in terms of RMS peak power and resonance frequencies should be computed for DOF 1 and 2.

$$err_{peak1,2}\% = \left| \frac{P_{model,peak1,2} - P_{exp,peak1,2}}{P_{exp,peak1,2}} \right| * 100 \tag{19}$$

$$err_{freq1,2}\% = \left| \frac{\omega_{model,res1,2} - \omega_{exp,res1,2}}{\omega_{exp,res1,2}} \right| * 100 \tag{20}$$

Table 4 reports the errors obtained for EH3 different coil connections. Coil 3 numerical FRF has a perfect match with experimental results for peak amplitude of the second resonance, whereas the first peak has a moderate error about 8%. The resonance frequencies errors for coil 3 are around 1%, hence are completely negligeable considering the strong non-linear behavior of the system. Coil 10 numerical FRF have a modest error of about 10% for the resonance frequencies due to the "hardening" impact behavior mentioned before. Nonetheless, coil 10 numerical peaks amplitudes match almost perfectly with the experimental results with errors of 0.4% and 3.1%. Coil 3–10 series has the overall best fitting results between model and experimental results, with almost zero errors both on peak amplitudes and resonance frequencies.

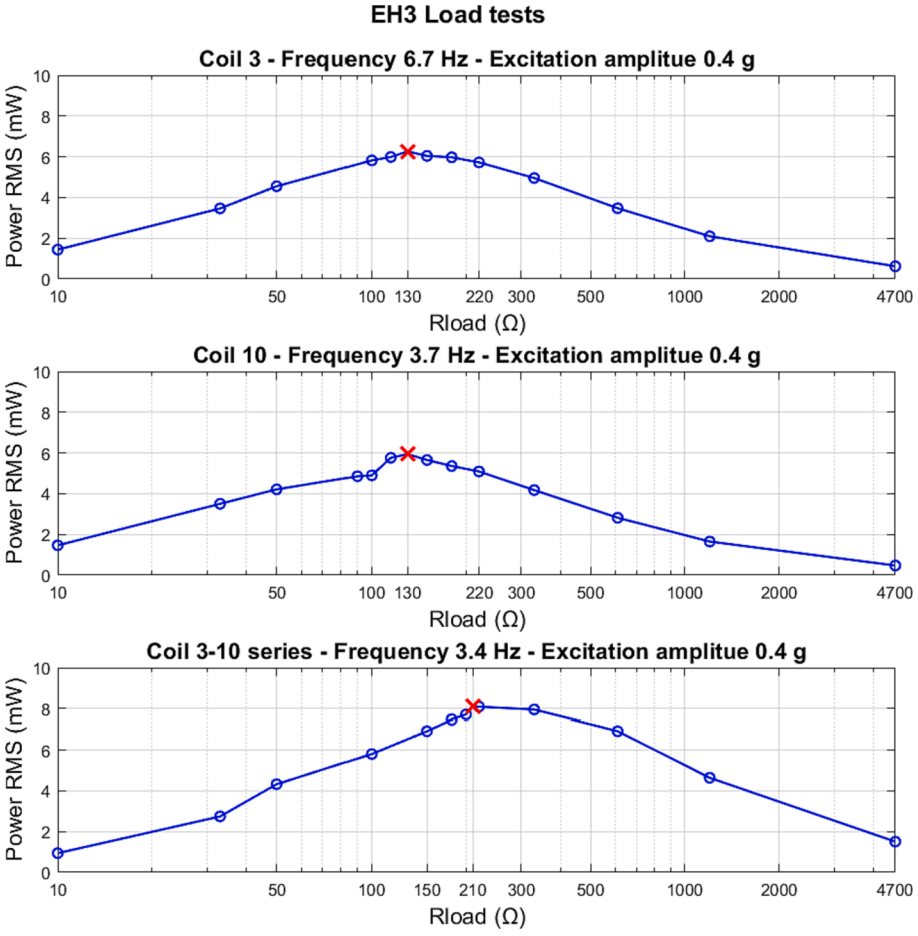

Fig. 17. Experimental load tests on EH3.

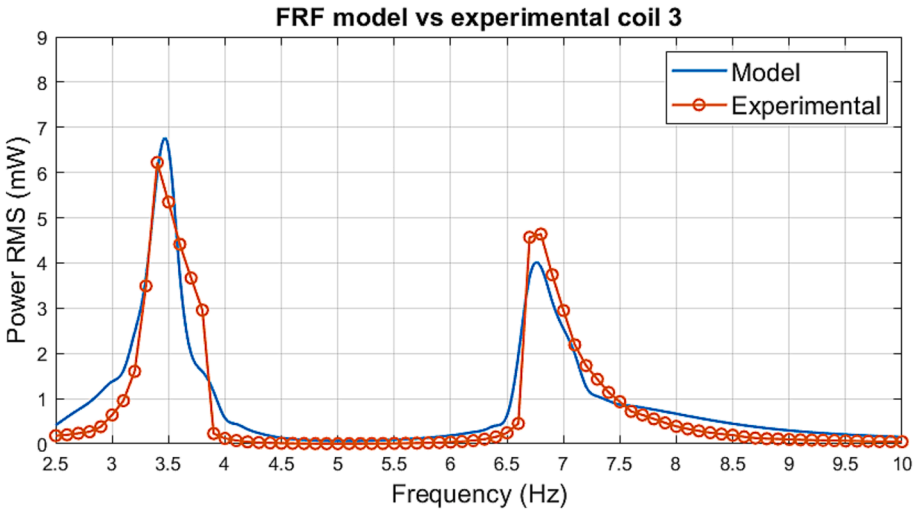

Fig. 18. Numerical and experimental FRFs comparison for EH3 coil 3 connection.

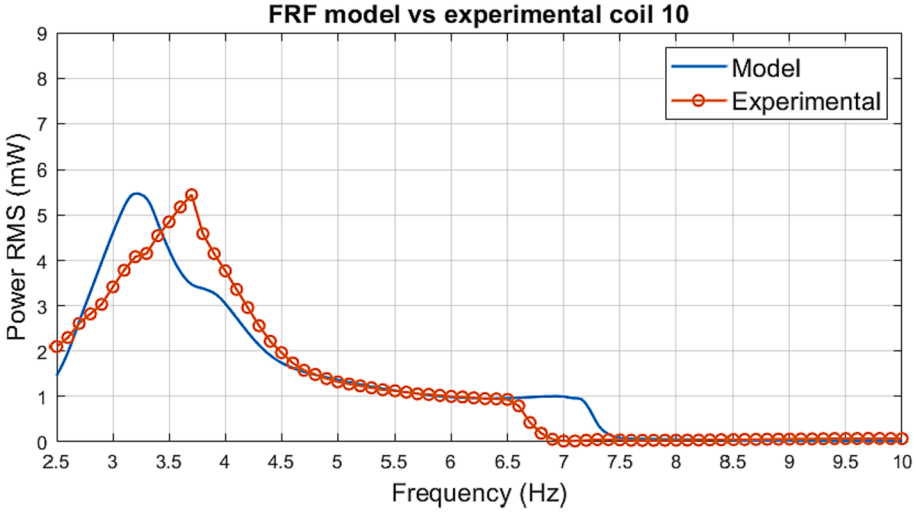

Fig. 19. Numerical and experimental FRFs comparison for EH3 coil 10 connection.

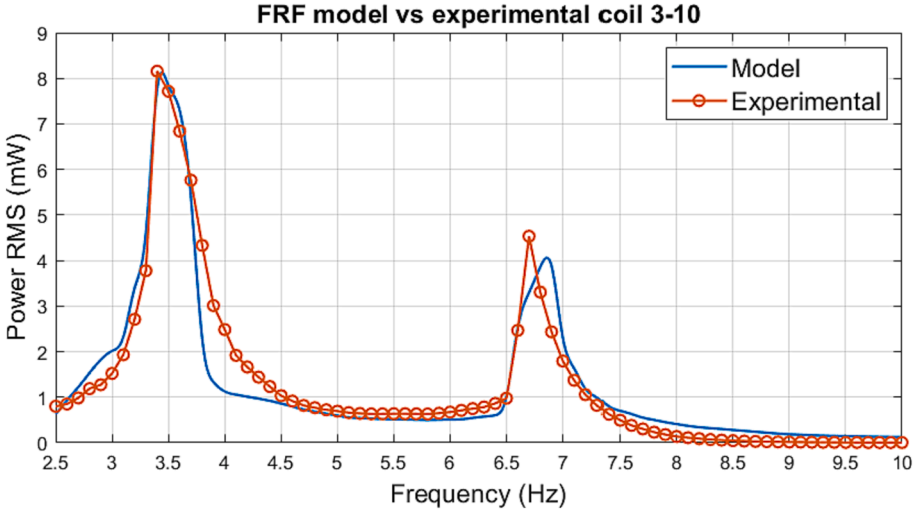

Fig. 20. Numerical and experimental FRFs comparison for EH3 coil 3–10 series connection.

Table 4
Peaks and resonance frequencies relative errors for EH3.

Coil connection	$err_{peak,1}$(%)	$err_{peak,2}$(%)	$err_{freq,1}$(%)	$err_{freq,2}$(%)
Coil 3	8.4	0	1.5	0.6
Coil 10	0.4	3.1	12.7	10
Coil 3-10 series	0.7	1.7	1.5	2.5

Table 5
Experimental index values for EH3 optimum coils series connection.

Coil connection	$I1_{peak}$	$I2_{peak}$	I_{AUC}
Coil 3-10 series	1	1	1
Coil 3	0.76	0.98	0.63
Coil 10	0.99	0.22	0.97

4. Discussions

4.1. Power enhancement with series connection of two coils

The main goal of using of two magneto-inductive masses is not only the frequency bandwidth broadening related to the introduction of another degree of freedom, but also the amplification of power generation. This result can be obtained by using a series connection of the two optimum coils, one for each moving magnet. Numerical simulations in Ansys Maxwell and MATLAB already prove the power increase of the series connection, as it is described in Section 2.2.2. Laboratory tests are performed to validate this behavior with experimental results. Fig. 21 shows the experimental RMS power FRFs of coil 3, coil 10 and their series connection.

The curve for coil 3 shows two high resonance peaks at 3.4 Hz and 6.8 Hz respectively of 6.1 mW and 4.7 mW, but when the harvester is excited with frequencies in the region in between the peaks the output power is almost zero. Coil 10 curve, on the contrary, has a high peak amplitude only for the first resonance frequency of 5.4 mW at 3.7 Hz, but generates a satisfactory amount of power also in the region in between the two resonance peaks. The series connection between the two coils has the purpose of combining the two strong points of each single coil to maximize the overall conversion efficiency. The series connection FRF shows high peak values of 8.2 mW and 4.3 mW at the resonance frequencies of 3.4 Hz and 6.7 Hz and a decent amount of power in the region in between the resonances, thus optimizing the AUC value. In order to quantify the power enhancement of the series connection, two indexes I_{peak} and I_{AUC} are computed as follows:

$$I1,2_{peak} = \frac{Peak1,2_{coil}}{Peak1,2_{series}} \tag{21}$$

$$I_{AUC} = \frac{AUC_{coil}}{AUC_{series}} \tag{22}$$

where:

- $Peak1,2_{coil}$, AUC_{coil} are the two resonance peaks and area under the curve of FRFs connecting single coils 3 or 10
- $Peak1,2_{series}$, AUC_{series} are the two resonance peaks and area under the curve of FRFs connecting coil 3 and 10 in series

Table 5 summarizes the experimental index values for EH3. The more these indexes are lower than 1 the worse is the performance of the single coil respect to the series connection. Connecting coil 3 leads to a significant reduction of the peak amplitude for DOF 1 and of the AUC. Coil 10 has a dramatic worsening of the peak amplitude for DOF 2 respect to the series connection. The results of this analysis lead to the conclusion that using two magneto-inductive masses with series connection of two coils consistently improves efficiency both in terms of peak amplitudes and AUC.

4.2. Performance comparison with 1DOF system

The advantages and disadvantages of a 2DOF GEMEH respect to a 1DOF system must be accurately studied to justify the design of a more complicated device.

As stated in Section 2.1, the fundamental design variable of 2DOF GEMEHs is the mass ratio between the two moving magnets, as it changes the device performances. For this reason, four different configurations having different mass ratios are experimentally tested on the dynamic workbench described in Section 2.3 and compared in terms of peak power and AUC. The configurations schematics are reported in Fig. 2 in Section 2.1. The FRFs are computed for each configuration applying an excitation input of 0.4 g amplitude, using optimum R_{load} and connecting the two optimum coils in series as it is explained in Section 2.2.2. The results of this analysis are shown in Fig. 22. Considering only the power generation as comparison term, EH4 shows the highest peak

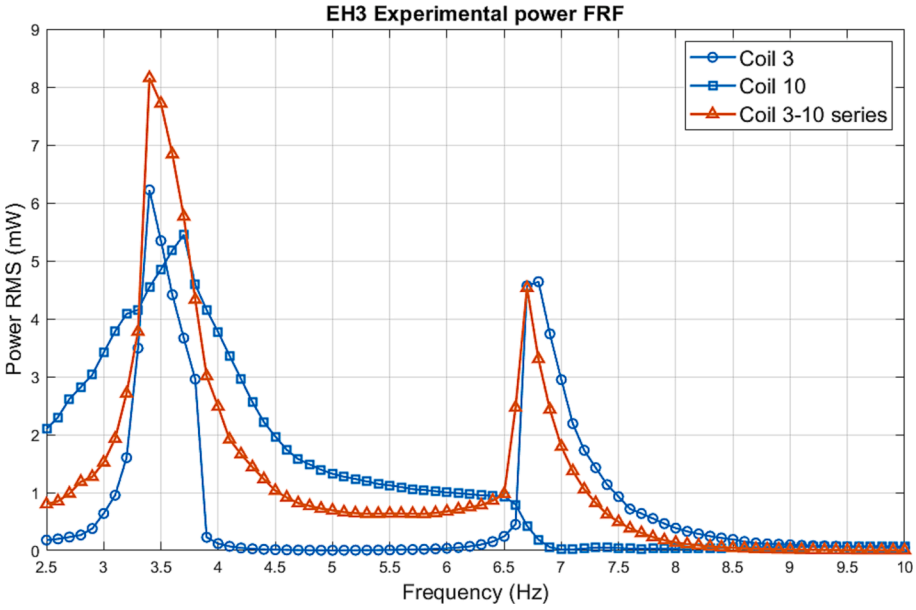

Fig. 21. Experimental FRFs for EH3 optimum coils series connection.

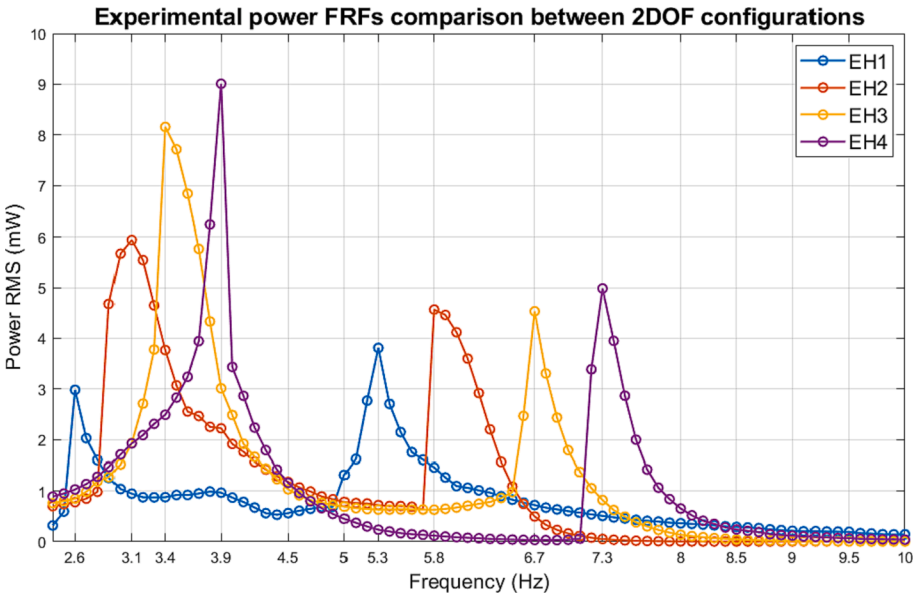

Fig. 22. Experimental FRFs comparison between 2DOF configurations.

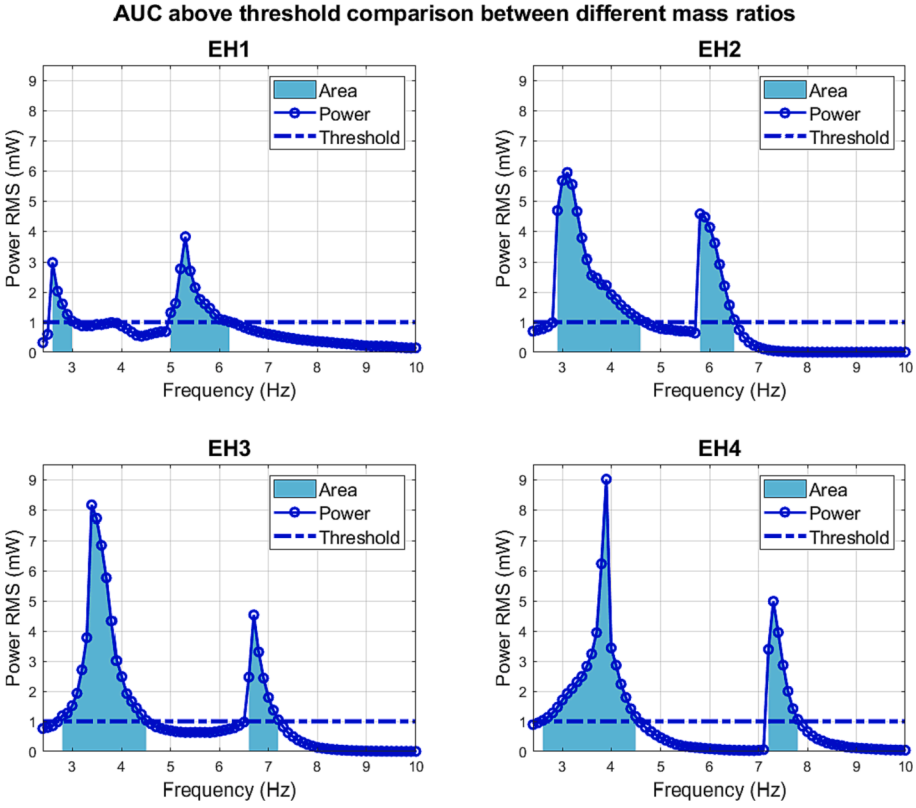

Fig. 23. Experimental AUC comparison between different mass ratios.

at resonance 1, while EH1 has the lowest peak. However, evaluating the peak power is not sufficient for a correct performance analysis of the devices. What must be taken into consideration is also the effective broadening of the high-power frequencies range. This can be quantified by computing the AUCs of the power FRFs in the regions where the generated power is above a certain threshold. This threshold should be the power consumption of the sensor node that the harvester supplies. However, the application of the device in supplying a real node regards future phases of the research. So, for this first performance analysis, a threshold equal to 1 mW is used because generated power under this value can be considered as noise and not relevant. AUC is a significant indicator as it depends both on peak amplitudes and frequency bandwidth. A merit factor considering the weights of both peak and AUC values is defined for a final performance evaluation and comparison. Fig. 23 shows the results of the AUC above the threshold comparison. Indexes must be defined in order to quantitatively compare the different configurations and find the one that enhances the performances the most respect to the 1DOF system. The merit factor and the indexes of

Table 6
2DOF-1DOF experimental comparison indexes.

Configuration	Max Peak (mW)	Bandwidth (Hz)[a]	I_{peak}	I_{band}	I_{AUC}	f_{merit}
1DOF	9.51	2.8	1	1	1	1
EH1	3.81	1.5	0.40	0.54	0.47	0.19
EH2	5.94	2.6	0.63	0.93	1.16	0.73
EH3	8.25	3.1	0.87	1.11	1.27	1.10
EH4	8.95	2.5	0.94	0.86	1.10	1.03

[a] Frequency bandwidth corresponding to power values above the threshold of 1 mW.

peak ratios, frequency bandwidth and AUC above the threshold are defined as follows:

$$I_{peak} = \frac{Peak_{2DOF}}{Peak_{1DOF}} \tag{23}$$

$$I_{band} = \frac{Bandwidth_{2DOF}}{Bandwidth_{1DOF}} \tag{24}$$

$$I_{AUC} = \frac{AUC_{2DOF}}{AUC_{1DOF}} \tag{25}$$

$$F_{merit} = I_{peak} * I_{AUC} \tag{26}$$

Table 6 summarizes the indexes results for the four tested configurations. The most important parameter for this performance analysis is the merit factor F_{merit} which has to be greater than 1 for effective performance enhancement respect to the 1DOF configuration. Increasing the mass ratio from EH1 to EH4, I_{peak} grows as expected, whereas I_{band} and I_{AUC} have the optimum values in EH3 configuration. EH2 has higher I_{band} and I_{AUC} than EH4 but minor I_{peak}, resulting in a F_{merit} value lower than 1. EH4 has the highest I_{peak} and F_{merit} greater than 1, however the poor I_{AUC} and I_{band} values are crucial in the final performance results. EH3 configuration has an increase in bandwidth of 11%, in AUC of 27% and has a merit factor of 1.10 respect to 1DOF system, admitting a peak power reduction of 13%. For this reasons, EH3 configuration has been chosen for the numerical model design and experimental validation. Fig. 24 shows the comparison between the optimum EH3 configuration and the 1DOF system in terms of experimental power FRFs with an excitation amplitude of 0.4 g. The 2DOF FRF curve has small amplitude in the region where the 1DOF system has its own natural frequency. Moreover, the two resonance peaks in the 2DOF system are smaller than the 1DOF peak due to the damping effect of the additional mass. However, the non-linear behavior of the two magnetic suspensions is not easily predictable as the linear dynamic absorber. The 2DOF GEMEH performances depend on the excitation amplitude and on the mass ratio, since it affects not only the resonance frequencies but also the output power. For these reasons, a detailed experimental study of the 2DOF GEMEH behavior with different mass ratios is necessary.

4.3. Performance comparison with devices in literature

Since the optimized configuration having the highest merit factor is identified, its performances can be compared to the ones of the similar 2DOF EMEHs in literature.

A fair comparison can be evaluated by computing the Normalized Power Density (NPD). The ratio between maximum power and device volume is normalized by the squared excitation amplitude imposed [28].

$$NPD = \frac{P_{max}}{(Y_0/g)^2 * Volume} \tag{27}$$

Table 7 shows the comparison results. The device studied in this paper presents the lowest resonance frequencies amongst the examined works, confirming its suitability for harvesting ultra-low frequency vibrations. The mediocre NPD value is due to the consistent height of the tube, since the top magnet m_2 needs a proper stroke to enhance power generation and have lower resonance frequency. The use of two co-axial magnetic springs in series causes m_2 to have an equilibrium position at significant distance from m_1, in particular of about 7 cm in EH3 configuration. Even though the power density is not optimal, the system still manages to generate a significant amount of power at ultra-low resonance frequencies. Moreover, the device comes with a novel, reliable and long-lasting design thanks to the two asymmetric magnetic springs series, while other researchers use more complex layouts and mechanical springs that have shorter durability and more design issues.

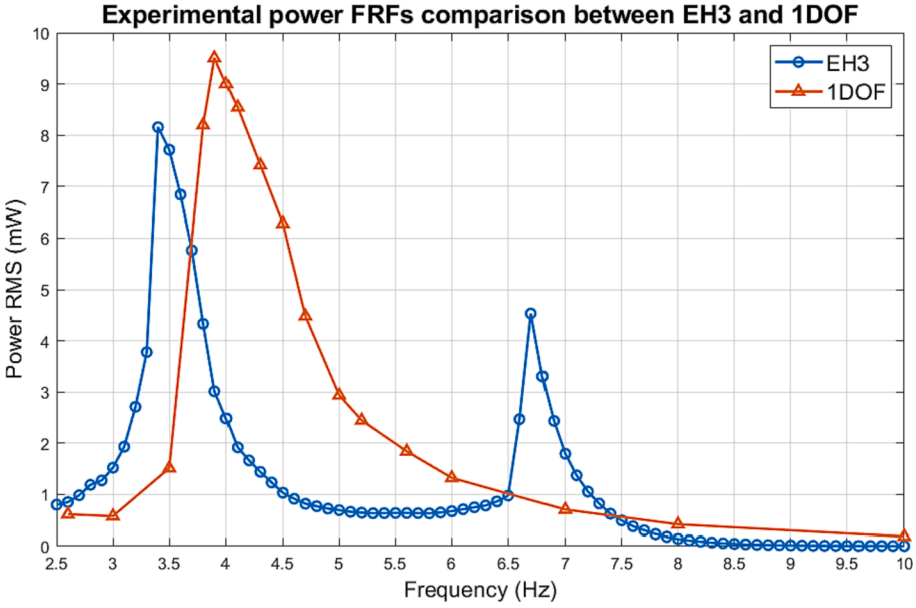

Fig. 24. Experimental FRFs comparison between EH3 and 1DOF system.

Table 7
Performance comparison with devices in literature.

Ref	Spring type	Res. Freq. (Hz)	Max. Power (mW)	Vol. (cm^3)	NPD ($mW/(cm^3 * g^2)$)
[18]	Planar	58, 74.5	39.8 @74.5 Hz, 0.45 g	53.9	2.77 @58 Hz, 0.27 g
[19]	Cantilever	4.4, 5.5	10.7 @5.5 Hz, 0.09 g	333	3.97 @5.5 Hz, 0.09 g
[20]	Helical	6.2, 14	25.0 @6.2 Hz, 0.31 g	800*	0.33 @6.2 Hz, 0.31 g
[12]	Helical	6.0, 14.6	218 @14.5 Hz, 0.40 g	600*	2.27 @14.5 Hz, 0.4 g
[17]	Magnetic	7.5, 18.5	2.58 @7.5 Hz, 0.50 g	9.73	1.06 @7.5 Hz, 0.5 g
[21]	Magnetic	7, 8, 9, 10	2.09 @8.5 Hz, 0.50 g	40.18	0.21 @8.5 Hz, 0.5 g
This work	Magnetic	3.4, 6.7	8.25 @3.4 Hz, 0.40 g	226	0.23 @3.4 Hz, 0.4 g

*Volume values are not explicitly reported in the paper but are estimated from magnets data.

5. Conclusions

The aim of this paper is to evaluate the performances of two-degrees-of-freedom gravitational electromagnetic energy harvesters. The novel design exploits the use of two magnetic suspensions in series, having two magneto-inductive masses and connecting two coils in series for maximum power generation. The purpose of this device is to enhance the power conversion efficiency of a simple 1DOF energy harvester by broadening the frequency bandwidth thanks to the introduction of a second resonance frequency. The presented systems are suitable for railway monitoring applications in freight trains, being able to scavenge ultra-low frequencies vibrations coming from the wheel-railroad contact to supply wireless sensor nodes. The potentiality of these devices is the possibility of tuning the two system natural frequencies to the fundamental excitation frequencies on the bogie frame when the railcar is loaded and unloaded, resulting in an increase of the power conversion efficiency. The device has a novel, efficient and more durable design respect to the ones proposed in literature, complying with the installation requirements of low maintenance and confirming its in-field applicability.

The performance analysis of the 2DOF GEMEHs requires a combined approach of numerical modeling and experimental laboratory tests. Different mass ratios for the two magnetic suspensions are experimentally tested in order to find the most efficient configuration compared to the analogous 1DOF system. Performance indicators are defined to have a quantitative comparison between the different configurations. EH3 configuration has the highest merit factor amongst all the tested prototypes, leading to a performance improvement of 10% respect to the 1DOF system. The frequency bandwidth corresponding to power values above the threshold of 1 mW increases of 11% and the power curve integral (AUC) of 27%. The two power peaks have values of 8.25 mW and 4.53 mW at the resonance frequencies of 3.4 Hz and 6.7 Hz respectively, applying an external excitation of 0.4 g. A numerical model of EH3 system is developed in MATLAB/Simulink and Ansys Maxwell environments to perform dynamics simulations. The numerical modeling approach is necessary to evaluate the stiffness and damping characteristics of the two magnetic suspensions due to their strong nonlinear behavior. The superimposition between numerical and experimental Frequency Response Functions leads to satisfactory results, hence validating the proposed harvester model. The series connection between the two optimum coils for each moving magnet leads to an increase of the output power peaks and AUC, confirming the advantages of using two magneto-inductive proof masses. The power density of the device is not optimal when compared to analogous systems in literature due to the long stroke given to the top mass m_2, however the low-maintenance long-lasting design, the valid performances of the 2DOF GEMEH and its in-field applicability overcome this drawback. The use of the two magnetic asymmetric suspensions in series results in a dynamic behavior of the system having the lowest resonance frequencies amongst the other literature works, confirming its suitability for the railway monitoring applications.

Future works must be focused on the development of the sensorized node for evaluation of the real power consumption in working conditions of the freight train. Moreover, the real fundamental excitation frequencies on the bogie hosting the harvester must be evaluated in order to precisely define the magnets mass ratio that tunes the system resonance frequencies when the railcar is loaded and unloaded.

CRediT authorship contribution statement

M. Lo Monaco: Conceptualization, Methodology, Software, Validation, Formal analysis, Investigation, Data curation, Writing - original draft, Writing - review & editing, Visualization. **C. Russo:** Conceptualization, Methodology, Software, Validation, Formal analysis, Investigation, Data curation, Visualization. **A. Somà:** Conceptualization, Validation, Resources, Supervision, Project administration, Funding acquisition.

Declaration of Competing Interest

The authors declare that they have no known competing financial interests or personal relationships that could have appeared to influence the work reported in this paper.

Data availability

Data will be made available on request.

References

[1] M. Shirvanimoghaddam, K. Shirvanimoghaddam, M. Abolhasani, M. Farhangi, V. Barsari, H. Liu, M. Dohler, M. Naebe, Paving the path to a green and self-powered internet of things; 2017.
[2] Majid M, Habib S, Javed AR, Rizwan M, Srivastava G, Gadekallu TR, Lin JCW. Applications of wireless sensor networks and internet of things frameworks in the industry revolution 4.0: A systematic literature review. Sensors 2022;22. https://doi.org/10.3390/s22062087.
[3] Singh J, Kaur R, Singh D. Energy harvesting in wireless sensor networks: A taxonomic survey. Int J Energy Res 2021;45:118–40. https://doi.org/10.1002/er.5816.
[4] Dewan A, Ay SU, Karim MN, Beyenal H. Alternative power sources for remote sensors: A review. J Power Sour 2014;245:129–43. https://doi.org/10.1016/j.jpowsour.2013.06.081.
[5] Pasquale GD, Somá A, Zampieri N. Design, simulation, and testing of energy harvesters with magnetic suspensions for the generation of electricity from freight train vibrations. J Comput Nonlinear Dyn 2012;7. https://doi.org/10.1115/1.4006920.
[6] Pasquale GD, Somá A, Fraccarollo F. Piezoelectric energy harvesting for autonomous sensors network on safety-improved railway vehicles. Proc Inst Mech Eng, Part C: J Mech Eng Sci 2012;226:1107–17. https://doi.org/10.1177/0954406211418158.
[7] Pasquale GD, Somá A, Fraccarollo F. Comparison between piezoelectric and magnetic strategies for wearable energy harvesting. J Phys: Conf Ser 2013;476. https://doi.org/10.1088/1742-6596/476/1/012097.
[8] Russo C, Monaco ML, Fraccarollo F, Somá A. Experimental and numerical characterization of a gravitational electromagnetic energy harvester. Energies 2021;14. https://doi.org/10.3390/en14154622.
[9] Russo C, Monaco ML, Somá A. Energy harvester duty cycle evaluation for railway vehicle health monitoring. IOP Conf Ser: Mater Sci Eng 2022;1214. https://doi.org/10.1088/1757-899x/1214/1/012046.
[10] Bosso N, Magelli M, Zampieri N. Application of low-power energy harvesting solutions in the railway field: a review. Vehicle Syst Dyn 2021;59:841–71. https://doi.org/10.1080/00423114.2020.1726973.
[11] Melnik R, Koziak S. Rail vehicle suspension condition monitoring - approach and implementation. J Vibroeng 2017;19:487–501. https://doi.org/10.21595/jve.2016.17072.

[12] Ung C, Moss SD, Chiu WK. Electromagnetic energy harvester using coupled oscillating system with 2-degree of freedom. Active and Passive Smart Structures and Integrated Systems 2015;9431:94312C. https://doi.org/10.1117/12.2084416.
[13] Wei C, Jing X. A comprehensive review on vibration energy harvesting: Modelling and realization. Renew Sustain Energy Rev 2017;74:1–18. https://doi.org/10.1016/j.rser.2017.01.073.
[14] Zhu D, Tudor MJ, Beeby SP. Strategies for increasing the operating frequency range of vibration energy harvesters: A review. Meas Sci Technol 2010;21. https://doi.org/10.1088/0957-0233/21/2/022001.
[15] O'Donoghue D, Frizzell R, Kelly G, Nolan K, Punch J. The influence of mass configurations on velocity amplified vibrational energy harvesters. Smart Mater Struct 2016;25. https://doi.org/10.1088/0964-1726/25/5/055012.
[16] Rodriguez J, Nico V, Punch J. A vibration energy harvester and power management solution for battery-free operation of wireless sensor nodes. Sensors 2019;19. https://doi.org/10.3390/s19173776.
[17] Fan K, Zhang Y, Liu H, Cai M, Tan Q. A nonlinear two-degree-of-freedom electromagnetic energy harvester for ultra-low frequency vibrations and human body motions. Renewable Energy 2019;138:292–302. https://doi.org/10.1016/j.renene.2019.01.105.
[18] Feng Z, Peng H, Chen Y. A dual resonance electromagnetic vibration energy harvester for wide harvested frequency range with enhanced output power. Energies 2021;14. https://doi.org/10.3390/en14227675.
[19] Ahmad M, Khan F. Two degree of freedom vibration based electromagnetic energy harvester for bridge health monitoring system. J Intell Mater Syst Struct 2021;32:516–36. https://doi.org/10.1177/1045389X20959459.
[20] Zhang R, Wang X, Shu H, John S. The effects of the electro-mechanical coupling and halbach magnet pattern on energy harvesting performance of a two degree of freedom electromagnetic vibration energy harvester. Int J Vehicle Noise Vibr 2018;14:124–46. https://doi.org/10.1504/IJVNV.2018.095175.
[21] Foisal A, Hong C, Chung G. Multi-frequency electromagnetic energy harvester using a magnetic spring cantilever. Sens Actuat A: Phys 2012;182:106–13. https://doi.org/10.1016/j.sna.2012.05.009.
[22] O'Donoghue D, Frizzell R, Punch J. Scaling and characterisation of a 2-dof velocity amplified electromagnetic vibration energy harvester. Smart Mater Struct 2018;27. https://doi.org/10.1088/1361-665X/aac297.
[23] Cottone F, Frizzell R, Goyal S, Kelly G, Punch J. Enhanced vibrational energy harvester based on velocity amplification. J Intell Mater Syst Struct 2014;25:443–51. https://doi.org/10.1177/1045389X13498316.
[24] Santos MPSD, Ferreira JAF, Simões JAO, Pascoal R, Torrão J, Xue X, Furlani EP. Magnetic levitation-based electromagnetic energy harvesting: A semi-analytical non-linear model for energy transduction. Sci Rep 2016;6. https://doi.org/10.1038/srep18579.
[25] Carneiro P, dos Santos MPS, Rodrigues A, Ferreira JAF, Simões JAO, Marques AT, Kholkin AL. Electromagnetic energy harvesting using magnetic levitation architectures: A review. Appl Energy 2020;260. https://doi.org/10.1016/j.apenergy.2019.114191.
[26] Fu WN, Zhou P, Lin D, Stanton S, Cendes ZJ. Magnetic force computation in permanent magnets using a local energy coordinate derivative method. IEEE Trans Magn 2004;40:683–6. https://doi.org/10.1109/TMAG.2004.824774.
[27] Kraftmakher Y. Magnetic field of a dipole and the dipole-dipole interaction. Eur J Phys 2007;28:409–14. https://doi.org/10.1088/0143-0807/28/3/003.
[28] Beeby SP, Torah RN, Tudor MJ, Glynne-Jones P, O'Donnell T, Saha CR, Roy S. A micro electromagnetic generator for vibration energy harvesting. J Micromech Microeng 2007;17:1257–65. https://doi.org/10.1088/0960-1317/17/7/007.